Journal of Materials Chemistry C

Two-Step Spin-Coating of Vacancy-Ordered Double Perovskites Enables Growth of Thin Films for Electronic Devices

Journal:	*Journal of Materials Chemistry C*
Manuscript ID	TC-ART-02-2025-000502.R1
Article Type:	Paper
Date Submitted by the Author:	07-Apr-2025
Complete List of Authors:	Kuklinski, Owen; University of California Santa Barbara, Materials Brumberg, Alexandra; Drexel University, Chemistry Tang, Linjing ; University of California Santa Barbara, Materials Mulligan, Anya; University of California Santa Barbara, Materials Kodalle, Tim; Lawrence Berkeley Laboratory, Molecular Chemistry Sutter-Fella, Carolin; E O Lawrence Berkeley National Laboratory, Seshadri, Ram; University of California, Materials Research Laboratory Chabinyc, Michael; University of California Santa Barbara, Materials

Two-Step Spin-Coating of Vacancy-Ordered Double Perovskites Enables Growth of Thin Films for Electronic Devices

Owen Kuklinski[1], Alexandra Brumberg[1,2], Linjing Tang[1], Anya S. Mulligan[1,2], Tim Kodalle[3], Carolin M. Sutter-Fella[3], Ram Seshadri[1,2] and Michael L. Chabinyc[1,*]

[1]Department of Materials, University of California, Santa Barbara, CA 93106, USA.

[2]Materials Research Laboratory, University of California, Santa Barbara, CA 93106, USA.

[3]The Molecular Foundry, Lawrence Berkeley National Laboratory, Berkeley, California 94720, USA.

Abstract

Vacancy-ordered double perovskites (VODPs), such as Cs_2TeX_6 (X = Cl, Br, I), are lead-free alternatives to conventional metal-halide perovskites (MHPs). One limitation of VODPs is the lack of processes to form thin films relevant for physical characterization and electronic devices. A two-step spin-coating method was developed for synthesizing high-quality films of Cs_2TeBr_6. Independently depositing CsBr and $TeBr_4$ enables high precursor concentration and control over crystallization dynamics. By optimizing spin-coating parameters, conversion of precursors to phase pure films was observed using structural and surface characterization methods. The growth of mixed-halide systems was investigated using alternative salts including CsCl and CsI. Formation of halide alloys was found to depend on the existence of routes to byproducts. Lastly, single carrier diodes of Cs_2TeBr_6 were designed following valence band characterization with photoelectron spectroscopy. Temperature-dependent space-charge-limited current measurements revealed that transport occurs by hopping and the hole mobility is 3.2×10^{-5} cm^2 V^{-1} s^{-1} near room temperature. The insights from the 2-step procedure provide a pathway towards making semiconducting devices from VODPs.

Introduction

The pressing demand for low-temperature, solution-processable semiconductors has driven a revolution in research on metal-halide perovskites (MHPs).[1,2] Three-dimensional (3D) MHPs have remarkable carrier lifetimes and diffusion lengths, resulting in high-performing semiconducting devices like solar cells, light-emitting diodes (LEDs), and sensors.[3–6] These materials have the formula ABX_3, where A is a monovalent organic cation, B is a divalent metal cation, and X is a halogen anion. Despite having impressive performance, many 3D MHPs exhibit poor stability.[7] Because of this, many studies have been conducted on lower-dimensional MHP systems (2D, 1D), where reduced corner-sharing of the BX_6 octahedra has been shown to reduce ion mobility and sensitivity to water thereby improving stability.[8–12] The B-site metal cation however remains prone to oxidation since it is divalent. Vacancy-ordered double perovskites (VODPs) of the form A_2BX_6 remedy this issue because the B-site cation is tetravalent and less prone to oxidation, or in some cases, in the maximum oxidation state, granting the material greater resistance against degradation in the ambient.[13,14] VODPs are considered zero-dimensional because the octahedra experience no corner-sharing and are relatively isolated from one another. Despite this structure, the relatively soft heavier halide anions still allow for disperse electronic bands. The unique geometry of these compounds, while advantageous for stability, welcomes a new suite of optical, electronic, and structural properties due to the molecule-like isolated octahedra.

A notable consequence of a vacancy-ordered lattice is enhanced carrier- and exciton-phonon coupling. The lack of connectivity between octahedra enables greater susceptibility to deformation upon formation of charge carriers or excitons, thereby leading to polaron formation after excitation.[15] Prior studies have shown that this strong interaction induces localized carriers and excitons that consequently affect emission pathways and carrier transport.[16,17] Experimentally observed broad emission have been attributed to the potential wells created by localized charges predicted by computation.[15,17–20] Several contradicting results on the electronic properties of various VODPs have also been published recently, complicating characterization and device design. For example, reported values of the bandgap for Cs_2TeBr_6 based on density function theory calculations have differed by over 1.5 eV.[21,22] In the case of carrier mobility measurements, we are not aware of space-charge-limited current (SCLC) measurements for VODPs. SCLC measurements of diodes can reveal transport behavior in thin films relevant for devices, providing a more pertinent understanding of charge carrier dynamics.[23,24] However, effective diode fabrication requires high-quality thin films and careful choice of transport materials and electrodes. The limited co-solubility of all-inorganic precursors for VODP formulations has

hindered film synthesis. These limitations and discrepancies motivated us to study new growth methods for VODPs.

The most common method for MHP film casting is one-step spin-coating, where precursors for a given perovskite are co-dissolved and spin coated onto a substrate followed by a thermal annealing treatment. This simple method typically produces uniform films, but it offers little control over crystallization kinetics. Additionally, the precursors for desirable MHP systems are often not sufficiently co-soluble to make one-step deposition methods viable.[25,26] Researchers have recently been investigating two-step deposition methods as a viable synthetic alternative for MHPs.[27,28] Here, the B-site metal precursor is independently spin coated to create a film which is then either immersed in a solution of the A-site metal precursor or spin coated again with this solution deposited onto the preexisting film. Two-step methods have been shown to reduce defects in both hybrid and all-inorganic MHP films, contributing to competitive device performance among other synthetic routes.[29]

In this work, we explore new routes to grow the Cs_2TeX_6 (X = Cl, Br, I) class of VODPs as thin films. These materials have a tetravalent B-site cation that reduces degradation of the perovskite due to oxidation. Herein, we report a two-step spin-coating method for fabricating high-quality films of Cs_2TeBr_6. The rapid crystallization of this material from precursors CsBr and $TeBr_4$ enables dynamic two-step spin coating with strong repeatability and precise control over film properties. We show that the quality of the resulting thin film is highly dependent on the conditions of both spin coating steps and careful use of structural characterization techniques is essential to verify full conversion of $TeBr_4$ in the reaction to Cs_2TeBr_6. This method is also adapted to investigate the formation of mixed halide phases with CsCl and CsI precursors. Lastly, we uncover valence band energetics and fabricate single-carrier devices for measuring mobility via SCLC experiments.

Methods

Chemicals

Cesium bromide (99% metals basis) was purchased from *Alfa Aesar*. Tellurium(IV) bromide (99% metals basis), acetone (certified ACS grade), and isopropyl alcohol (99.5%) were purchased from *Thermo Fisher Scientific*. Methanol (≥99.9%) was purchased from *Sigma-Aldrich*. Ethylene glycol (≥99%) was purchased from *VWR Chemicals BDH*.

Precursor Solutions

CsBr solution was made by dissolving purified CsBr in ethylene glycol at a target concentration of 1 M. $TeBr_4$ solution was made by dissolving $TeBr_4$ in methanol at a target concentration of 1 M. Solutions were heated at 50°C and stirred for 2 hours to ensure complete dissolution.

Two-Step Sequential Spin-Coating

Z-cut quartz and ITO/quartz substrates were purchased from *University Wafer*. Substrates were cleaned with sonication in water, acetone, and isopropyl alcohol for 10 minutes each, followed by an air plasma treatment for 10 minutes. In an N_2 glovebox, 50 uL of $TeBr_4$ solution was spin-coated at 500 rpm for 10 seconds and then ramped up to a speed between 2000 and 8000 rpm for 30 seconds, depending on desired thickness. The resulting film was annealed at 100°C for 5 minutes. After the first annealing step, the film was re-spun at 2000 rpm for 30 seconds. Once ramping to 2000 rpm was complete, 50 μL of the CsBr solution was deposited on top of the $TeBr_4$ film to form Cs_2TeBr_6. The final film was annealed again at 100°C for 5 minutes.

Powder X-Ray Diffraction

Powder X-ray diffraction patterns were collected with a Panalytical Empyrean Powder Diffractometer in reflection mode. Cu Kα_1 was used as the X-ray radiation source with an accelerating voltage of 45 kV and beam current of 40 mA. Scans were performed from $2\theta = 3°$ to $2\theta = 60°$ with a step size of 0.04° and step time of 40 ms.

UV-Vis

A Shimadzu UV3600 UV-Vis-NIR Spectrometer was used to collect diffuse reflectance spectra. Scans were performed from 300 to 900 nm with a step size of 0.5 nm. Reflectance data was converted to absorbance with the Kubelka-Munk transform. Tauc plots for indirect band gap materials were generated to determine the band gap with a linear fit of the absorption edge.

Photoluminescence

Emission spectra was collected in reflectance mode with a 430 nm long pass filter, spectrometer, and visible CCD detector. Samples were excited at 405 nm with a continuous wave laser diode.

Grazing incidence wide-angle X-ray scattering (GIWAXS)

GIWAXS experiments were performed at Stanford Synchrotron Radiation Lightsource (SSRL) on beam line 11-3, which has a fixed energy of 12.7 keV and is equipped with a two-dimensional Rayonix MX225 CCD area detector. Lanthanum hexaboride (LaB_6) was used to refine the beam center and sample-to-detector distance. Data was collected with an incidence angle of 3° to access

a large range in q. Geometric corrections to the raw images were made using Nika. Data was azimuthally integrated with WAXStools.

Scanning Electron Microscopy (SEM)

SEM images were collected with a Thermo Scientific Apreo C LoVac SEM. Films were mounted onto SEM stubs with double-sided copper tape and imaged with accelerating voltages of 5.00 kV and beam currents of 0.40 nA.

Ultraviolet and X-ray Photoelectron Spectroscopy

Ultraviolet photoelectron spectroscopy (UPS) and X-ray photoelectron spectroscopy (XPS) experiments were performed with a Thermo Scientific ESCALAB Xi^+ XPS Microprobe. For UPS experiments, before film casting, 20 nm of chromium followed by 90 nm of gold were deposited by thermal evaporation onto quartz substrates so that films did not experience charging. Cs_2TeBr_6 films were cast with an initial $TeBr_4$ layer spun at 8000 rpm so that the film was sufficiently thin to prevent charging issues. Nickel tape was adhered to the surface of the film and wrapped around the edge of the substrate to further assist with charge dissipation. A helium I radiation source was used, performing 5 scans with a pass energy of 1.5 eV, dwell time of 150 ms, and energy step size of 0.05 eV. Additional low energy scans were conducted with electron charge compensation to ensure that sample charging didn't alter the onset, aligning with data collected without compensation. A corrected helium I satellite line background was subtracted using CasaXPS. For XPS experiments, X-rays were generated with a monochromated aluminum anode (1486.7 eV). Scans were performed with a pass energy of 100 eV, dwell time of 20 ms, and energy step size of 0.5 eV. Charge compensation was applied, and charge shift was accounted for by calibrating to trace oxygen photoemission at 531 eV. Thermo Scientific Avantage Data System was used to fit peaks with a Smart background and quantify atomic percentages.

Device Fabrication and Testing

Device architecture is pictured in **Figure 6a**. Cs_2TeBr_6 was deposited onto indium tin oxide (ITO) coated glass substrates through two-step spin coating. $TeBr_4$ was spun at 4000 rpm, followed by 1.5 M CsBr at 2000 rpm. 20 nm of molybdenum (VI) oxide (MoO_3) followed by 100 nm of gold were thermally evaporated in high vacuum and deposited onto the Cs_2TeBr_6 film through a mask to form mm^2 contacts. Devices were tested with a LakeShore Cryogenic Vacuum Probe Station and Keithley 2400 SourceMeter. Current-voltage scans were performed with a step size of 0.05 V.

Results

Synthesis and Film Casting

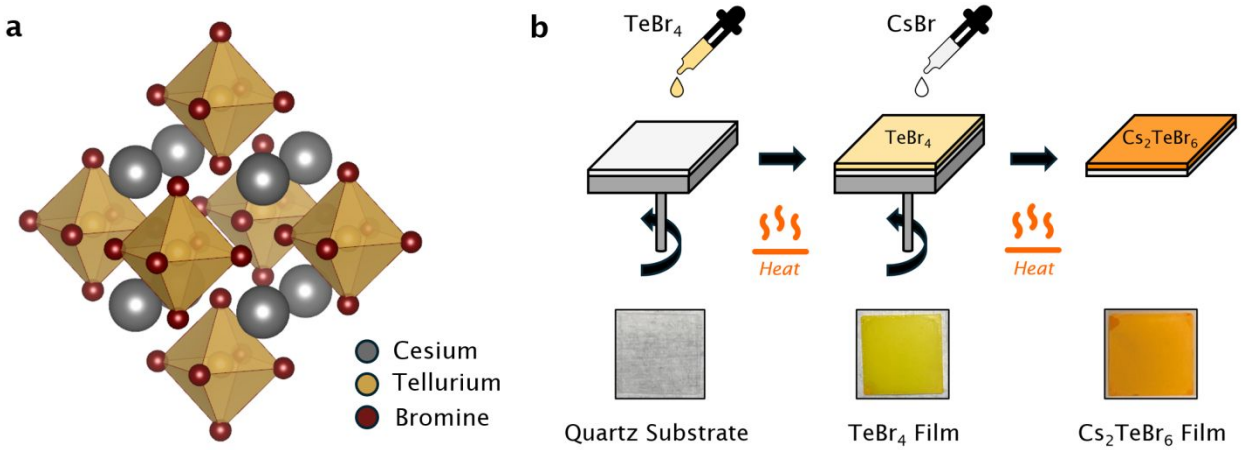

Figure 1: (a) Crystal structure of Cs_2TeBr_6, depicting characteristic isolated octahedra of VODPs. (b) Schematic of two-step spin-coating procedure for Cs_2TeBr_6 films and corresponding photographs of the resulting films. The films shown are on 15 mm x 15 mm quartz substrates.

The reported growth procedures for thin films of VODPs have been limited in comparison to higher-dimensional MHPs. In the case of Cs_2TeX_6 (**Figure 1a**), its bulk powder dissolves with a polar aprotic solvent into Cs^+ cations and $[TeX_6]^{2-}$ anions, producing solution that is highly stable. Drop-casting and pad printing have been demonstrated to form films of Cs_2TeX_6.[30] Drop cast films frequently suffer from defects, such as pinholes or variations in thickness, that form as the solvent evaporates upon casting.[31] In contrast, spin-coating can alleviate inhomogeneity and provide greater control over grain size, thickness, and other film properties.[32] Producing high quality films via spin coating depends on numerous factors, including the spin speed, concentration and the viscosity of precursor solution, and annealing procedure. The relatively low solubility of Cs_2TeX_6 (0.125 M) in polar aprotic solvents, like dimethylformamide (DMF) and dimethyl sulfoxide (DMSO), however makes it a challenge to spin-coat uniform and continuous thin films. Our attempts at spin coating films of Cs_2TeX_6 with DMSO and DMF solutions resulted in virtually no material being retained on the substrate due to the low concentration of the solution. Typically, minimum concentrations of ≈30 wt% are desirable for MHP films.[33] This difficulty suggested the need to examine other routes to form thin films of VODPs.

The simple, rapid reaction between a cesium halide salt and tellurium metal complex (**Equation 1**) encouraged us to investigate two-step spin coating as a potential route for producing high-quality continuous films.

$$2\ CsX + TeX_4 \rightarrow Cs_2TeX_6$$

Equation 1: The balanced chemical reaction between cesium halide salt (CsX) and tellurium tetrahalide (TeX_4) to form the target cesium tellurium VODP.

Casting a perovskite film with two deposition steps adds complexity to the overall procedure relative to using a single precursor. The spin-coating parameters must be carefully optimized such that the two reactants completely convert into the desired perovskite phase while still producing a film that is free of morphological defects. Most importantly, the first layer must not be soluble in the solvent of the second precursor solution or else the entire film will wash off the substrate. Solvent choice and sequence of casting therefore play a critical role in developing a successful procedure. Two-step studies with lead iodide perovskites cast the PbI_2 layer first because it does not degrade upon annealing and readily crystallizes to form a film.[27] We took a similar approach and deposited the metal halide TeX_4 in the first layer **(Figure 1b)**. In the case of the bromine derivative, methanol is an effective solvent choice for $TeBr_4$ because of its solubility at room temperature. Ethylene glycol was found to rapidly dissolve CsBr at concentrations as high as 2 M, but not $TeBr_4$, determining the order of the two-step process. We rationalize this slow dissolution with the characteristic viscosity of ethylene glycol. The conversion of $TeBr_4$ to Cs_2TeBr_6 is proposed to proceed by the dissociation of $(TeBr_4)_4$ clusters into $[L_2TeBr_3]^+Br^-$ solvent-coordinated complexes followed by reaction with the metal halide salt (see Supporting Information for the reaction steps).[34–36] Thus, we deduce that ethylene glycol can successfully coordinate with $TeBr_4$ to form these intermediate complexes when CsBr solution is deposited, but the higher viscosity relative to other solvents slows down dissolution considerably. As a result, the $TeBr_4$ film is not completely dissolved and washed away during deposition.

We examined different deposition processes to investigate the two-step growth process. In solution-based two-step procedures, growth of the final material is initiated by either immersing the first layer in a precursor solution or by depositing a precursor solution onto the first layer before, or during, spinning. These are referred to as immersion, static spin-coating, and dynamic spin-coating, respectively.[27] In our case, adding CsBr via static spin-coating and immersion resulted in patchy, irregular films with residual CsBr observed by powder X-ray diffraction (PXRD). These methods expose the $TeBr_4$ film to a significant excess of CsBr which is then incorporated into the sample. In contrast, dynamically depositing the second layer limits the amount of CsBr available to react because the volume of liquid on top of the substrate is determined by the spin speed. Depositing CsBr solution while spinning therefore prevents residual CsBr in the final film. This stoichiometric control is enabled by the rapid kinetics of the

reaction between CsBr and $TeBr_4$. Films are annealed after each deposition step to promote crystallization and remove solvent, but the reaction between CsBr and $TeBr_4$ commences immediately upon deposition, evident by a stark color change.

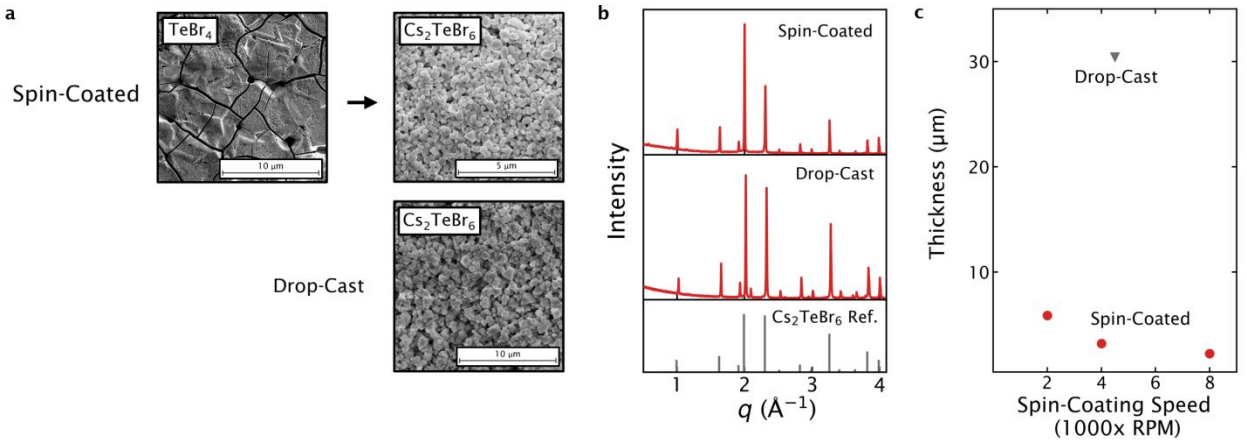

Figure 2: (a) SEM images of $TeBr_4$ and Cs_2TeBr_6 films made via two-step spin-coating procedure (top) and drop-casting (bottom). Drop-cast film was made by dropping 200 uL of 0.125 M Cs_2TeBr_6 solution onto a quartz substrate at 170°C. 50 uL of toluene was deposited in tandem as an anti-solvent. Spin-coated film was made by spinning 50 uL of 1 M $TeBr_4$ at 2000 rpm followed by 50 uL of 1 M CsBr deposited dynamically at 2000 rpm. (b) PXRD patterns for spin-coated Cs_2TeBr_6 film (top), drop-cast Cs_2TeBr_6 film (middle), and ICSD #24151 Cs_2TeBr_6 reference pattern (bottom). (c) Profilometer thickness data of films made via drop-casting and spin-coating. The spin-coating speed refers to the procedure for the initial $TeBr_4$ layer, which primarily influences final film thickness.

The fabrication method significantly influences the morphology, phase purity, and thickness of Cs_2TeBr_6 films. Scanning electron microscopy (SEM) images reveal morphological differences between films made via two-step spin-coating and drop-casting (**Figure 2a**). The initial $TeBr_4$ film, spun at 2000 rpm, has large cracks that separate highly porous domains. The porosity likely prevents the formation of a capping layer when CsBr is deposited because the solution can completely permeate the $TeBr_4$ layer and react. The resulting films have mostly spherical grains that are smaller than the octahedral crystallites found in drop-cast films. PXRD experiments indicate that two-step spin coating produces Cs_2TeBr_6 films with higher phase purity than drop-cast films (**Figure 2b)**. Diffraction patterns were compared to ICSD #24151 for Cs_2TeBr_6 in the Inorganic Crystal Structure Database (ICSD) to confirm the identity and purity of samples. PRXD spectra for drop-cast samples show excess CsBr present in the films given the (110) reflection at $q = 2.07$ Å^{-1}, which is the strongest reflection in CsBr reference spectra (ICSD #236387).

Conversely, the PXRD spectra for spin-coated films indicate phase-pure Cs_2TeBr_6 with no missing or additional reflections when compared to the ICSD reference. Changing the spin speed of the $TeBr_4$ layer dramatically alters the final thickness of the Cs_2TeBr_6 film. By varying the $TeBr_4$ spin speed between 2000 and 8000 rpm and depositing CsBr solution at 2000 rpm, the final film thickness can be tuned between roughly 2 and 5 microns (**Figure 2c, Figure S1**). This is in stark contrast to drop-cast films, which are limited to substantial thicknesses of about 30 microns. Thickness control is one of the key advantages of adopting spin-coating methods for MHP films.

The two-step spin-coating procedure introduces many process variables that impact film quality and phase purity. Conditions like the spin speed of both layers and concentration of precursor solution interact in complex ways, making optimization challenging. In addition, bulk characterization techniques may not fully capture the nuances of Cs_2TeBr_6 growth within these films. To follow the film evolution, *in-situ* photoluminescence experiments were conducted. The photoluminescence quantum yield (PQLY) of Cs_2TeBr_6 is sufficiently low that no emission is observed when exciting at 405 nm at a reasonable acquisition time, so the two-step procedure was amended to grow Cs_2TeCl_6 on glass substrates (see *Mixed Halide Compositions* section for more details). Cs_2TeCl_6 has a higher PLQY due to the greater ionicity of Te-Cl bonds causing flatter band dispersion.[35] In addition, the 3D Pb-containing $CsPbBr_3$ films were also synthesized in two steps by dissolving $PbBr_2$ in DMF to compare VODP growth to that of 3D structures. *In-situ* photoluminescence data collected during Cs_2TeCl_6 and $CsPbBr_3$ film casting at room temperature highlights the rapid reaction of precursors in two-step spin-coating. Characteristic Cs_2TeCl_6 emission centered around 2.05 eV was observed immediately upon deposition of CsCl onto $TeCl_4$ (**Figure S2**).[37] $CsPbBr_3$ emission was initially centered around 2.40 eV but gradually red shifted to 2.37 eV during spin-coating. This behavior has been attributed to quantum confinement and is possibly not observed in Cs_2TeCl_6 because of the molecular nature of VODPs.[38] The described observations hint at different growth mechanism but the degree of TeX_4 conversion as well as crystal phase evolution are not revealed with optical characterization. We therefore turned to grazing-incidence wide-angle X-ray scattering (GIWAXS) to understand how different processing parameters influence the composition of the resulting films.

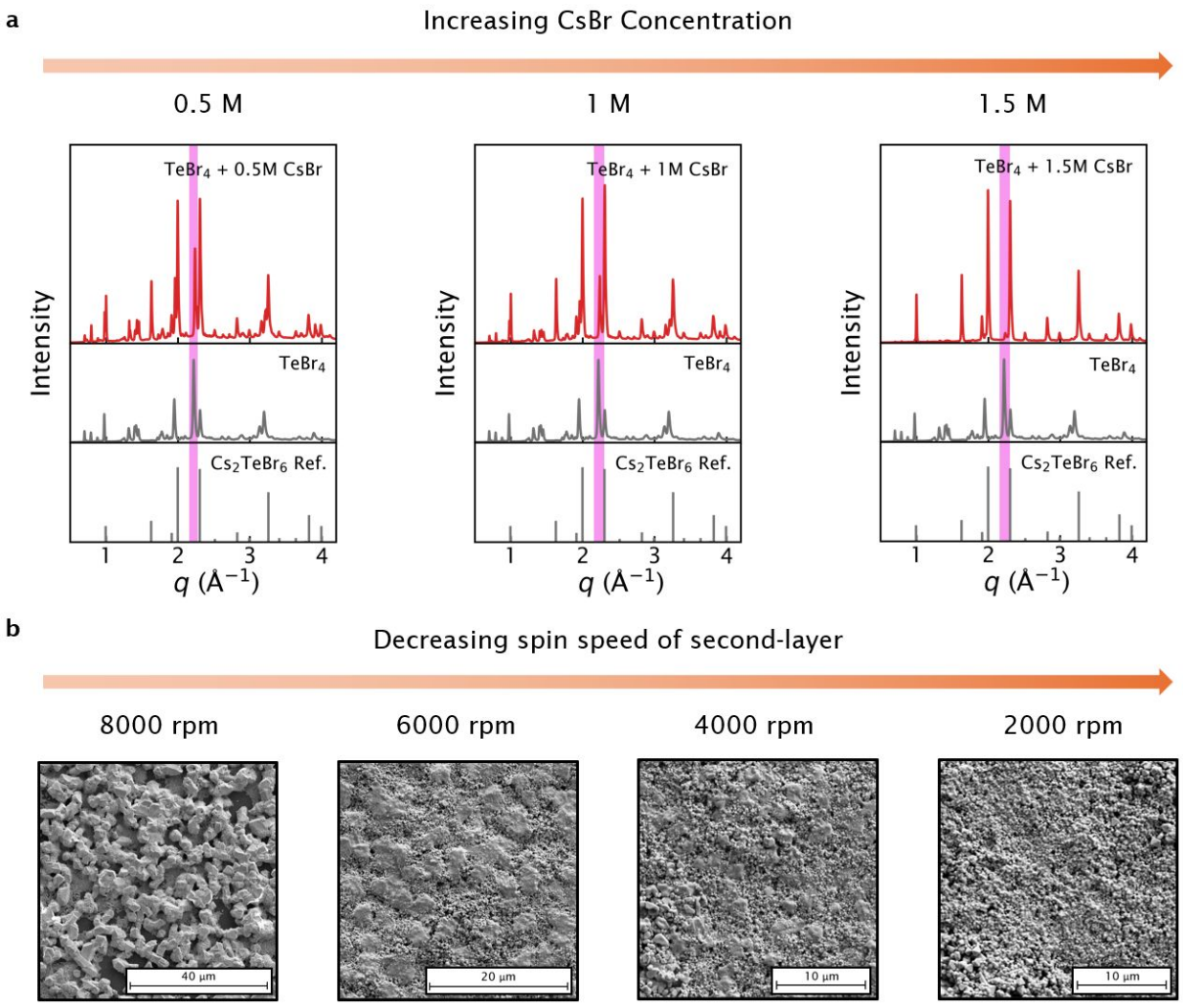

Figure 3: (a) Azimuthally integrated GIWAXS data collected at a 3° incidence angle of Cs_2TeBr_6 films made by depositing 0.5 M, 1 M, and 1.5 M CsBr solution (top) in two-step spin-coating procedure. $TeBr_4$ pattern (middle) and ICSD 24151 reference pattern (bottom) are included for peak assignment. The pink shaded region marks the most prominent $TeBr_4$ reflection. (b) SEM images of Cs_2TeBr_6 films made with varying CsBr deposition spin-speeds.

The detailed influence of the concentration of CsBr solution required to form Cs_2TeBr_6 is best evaluated using GIWAXS. While laboratory PXRD provides a fingerprint of crystalline phases in the bulk of a film, GIWAXS provides access to a wider region of reciprocal space and can selectively probe different sample depths by varying the grazing-incidence angle.[39] The higher brilliance of synchrotron X-ray sources also enables detection of weakly scattering phases that are not easily visible with PXRD. Films made with different concentrations of CsBr were characterized with GIWAXS to determine ideal synthetic conditions for phase-pure samples (**Figure 3a**). None of the Cs_2TeBr_6 films analyzed with GIWAXS exhibit significant texturing

through the depth (**Figure S3**), as the 2D diffraction patterns exclusively display rings without any discernible peaks indicating orientation. Phase information was therefore compared to powder reference patterns by azimuthally integrating the diffraction patterns to generate 1D scattering patterns. Unlike PXRD patterns, residual $TeBr_4$ is detectable with GIWAXS given the presence of reflections that match a collected GIWAXS pattern for a $TeBr_4$ film. The lack of sensitivity to $TeBr_4$ in PXRD patterns is due to residual $TeBr_4$ primarily populating the surface of the film that is more easily revealed with GIWAXS. This is made clear by the increasing intensity of $TeBr_4$ reflections relative to Cs_2TeBr_6 reflections as the grazing-incidence angle decreases (**Figure S4**) and is further supported by X-ray photoelectron spectroscopy (XPS) that shows excess tellurium on the surface of films (**Figure S5, S6, Table S2, S3**). *In-situ* photoluminescence data demonstrated that when TeX_4 reacts with CsX, Cs_2TeX_6 rapidly precipitates, leaving unreacted $TeBr_4$ to be coordinated with ethylene glycol in the liquid layer. Solvent is then evaporated during annealing and residual $TeBr_4$ is left on the surface of the Cs_2TeBr_6 film. Increasing the concentration of CsBr solution deposited onto $TeBr_4$ results in diminished presence of $TeBr_4$ reflections in GIWAXS and increased intensity of Cs_2TeBr_6 reflections, highlighting greater $TeBr_4$ conversion. The most prominent reflection attributed to $TeBr_4$ in GIWAXS is at q = 2.22 $Å^{-1}$ (highlighted with pink shading in **Figure 3a**) and its diminishing presence in Cs_2TeBr_6 patterns best illustrates this concentration dependence. In addition, no reflections expected from CsBr are observed (**Figure S7**).

The spin speed during deposition of CsBr was optimized for growth of phase pure films and to minimize any residual $TeBr_4$ on the surface. After successfully producing films at 2000 rpm, higher spin speeds were tested to vary the film thickness. To our surprise, films made by spin-coating both layers at higher spin speeds had an overwhelming residual $TeBr_4$ presence in integrated GIWAXS patterns despite a thinner $TeBr_4$ layer (**Figure S8**). This suggests that the spin speed of the second layer is a crucial factor in the conversion to Cs_2TeBr_6, which was further studied with SEM experiments (**Figure 3b**). Films with the $TeBr_4$ layer cast at 8000 rpm and subsequent CsBr depositions at 2000 rpm, 4000 rpm, 6000 rpm, and 8000 rpm were made and imaged with SEM. Higher spin-speed films show unreacted $TeBr_4$ crystallites that dominate the substrate surface. As the second-layer speed decreases, the surface is further populated with Cs_2TeBr_6 crystallites in tandem with the disappearance of the large $TeBr_4$ domains. This same behavior is observed in films made at lower $TeBr_4$ spin speeds (**Figure S9**). The CsBr liquid layer on top of $TeBr_4$ is made thinner at higher spin speeds, limiting the amount of CsBr available to react and form perovskite. This result indicates that the thickness of the final Cs_2TeBr_6 must be

controlled dominantly by varying the speed of the initial $TeBr_4$ layer. Thickness variation was achieved by spin-coating $TeBr_4$ at 2000 rpm, 4000 rpm, and 8000 rpm followed by CsBr at 2000 rpm for all samples.

Using this data, we can estimate the thickness of the CsBr liquid layer which, along with concentration, largely determines the extent of conversion to the perovskite. Given that GIWAXS shows very little remaining $TeBr_4$ when depositing 1.5 M CsBr solution onto a $TeBr_4$ film spun at 2000 rpm, we can assume 100% yield at this concentration to estimate the thickness of the second liquid layer when spinning at 2000 rpm. We estimate a thickness of ≈40 μm with these process parameters, informing the conditions required to induce full conversion in the film (see Supporting Information).

Mixed-Halide Compositions

After successfully producing Cs_2TeBr_6 films via the two-step method, the procedure was adapted to determine if Cs_2TeCl_6 and Cs_2TeI_6 could also be grown. To form these materials, CsCl/CsI and $TeCl_4$/TeI_4 were used in place of CsBr and $TeBr_4$, respectively. $TeCl_4$ was similarly dissolved in methanol at 1M, while TeI_4 was dissolved in dimethyl formamide (DMF) due to poor solubility in methanol. CsCl and CsI were both dissolved in ethylene glycol at 1M. While the two-step method still formed the target phase on quartz substrates (**Figure S10**), the coverage was poor and most of the substrate was left bare. Unlike $TeBr_4$, $TeCl_4$ and TeI_4 are susceptible to sublimation and degradation, respectively, during the first annealing step. $TeCl_4$ has been shown to have an appreciable vapor pressure at 100°C and given the thin films here sublimation is likely, while TeI_4 decomposes to Te(s) and I_2(g) at even lower temperatures.[40,41] In contrast, $TeBr_4$ is more stable and decomposes to $TeBr_2$(g) and Br_2(g) at temperatures above 400°C.[42] Annealing $TeCl_4$ and TeI_4 at lower temperatures gave better results but the samples were still not continuous films. If annealing the first layer is skipped entirely, the desired product forms on the substrate but most washes off after depositing the cesium salt. While the inability to form pure phases with chloride and iodide limit the method, the stability of $TeBr_4$ suggested a route to form mixed halide compositions.

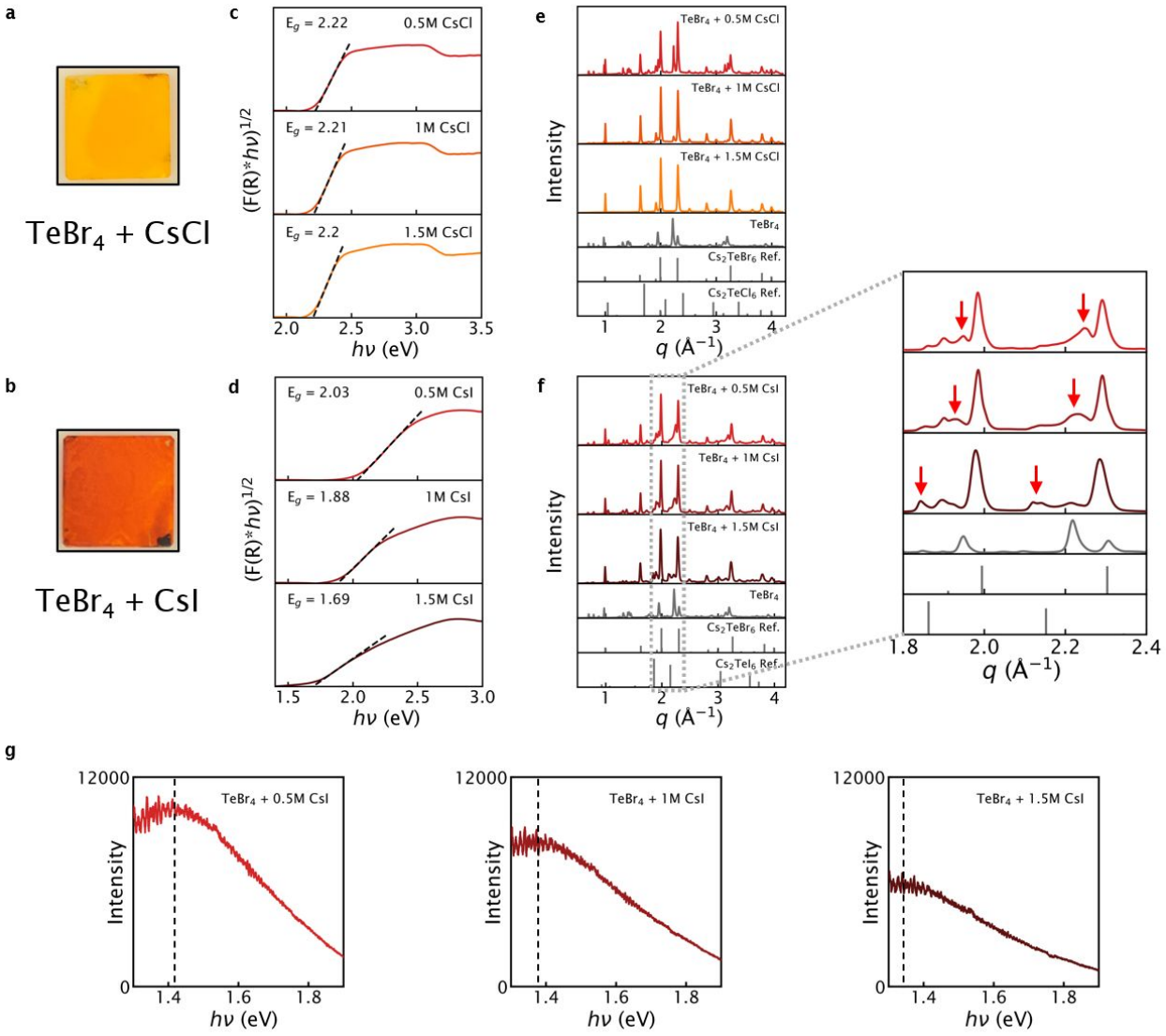

Figure 4: (a, b) Pictures of films made by depositing (a) CsCl and (b) CsI on top of initial $TeBr_4$ layer. (c, d) Tauc plots generated from UV-Vis reflectance data for films made by depositing (c) CsCl and (d) CsI solutions of varying concentrations with calculated bandgaps. (e) Azimuthally integrated GIWAXS data of films made with increasing CsCl concentration and ICSD 24151, ICSD 29031, and $TeBr_4$ patterns for reference. (f) Azimuthally integrated GIWAXS data of films made with increasing CsI concentration and ICSD 24151, ICSD 38105, and $TeBr_4$ patterns for reference. (g) Photoluminescence of films made with increasing CsI concentration, excited at 405 nm.

Multi-halide alloys provide means to tune the electronic properties of a given material and we targeted compositions that would show clear shifts in optical properties.[22,43,44] Our two-step spin-coating procedure was adapted by depositing CsCl and CsI at concentrations of 0.5 M, 1 M, and 1.5 M in the second step to react with $TeBr_4$ films (**Figure 4a, b**). Tauc plots of UV-Vis

reflectance data for these films reveal that the optical absorbance can be modified by the choice of halide salt.[45,46] Films made with CsI show a shift in the absorbance onset and optical band gap to lower energy as the concentration of deposited CsI solution increases. However, films made with CsCl show no difference in UV-Vis spectra and are all relatively identical to the spectra of Cs_2TeBr_6 (**Figure 4c, d**).

These films were analyzed with GIWAXS to determine the structure and composition after reacting with CsCl and CsI. As was done with Cs_2TeBr_6, GIWAXS data was azimuthally integrated to compare with reference powder patterns (**Figure 4e, f**, **Figure S5**). Diffraction patterns of films made with CsCl reveal that Cs_2TeBr_6 is the only compound formed, with no deviation in reflections from the Cs_2TeBr_6 reference pattern. This is consistent with the optical data which appears identical to that of Cs_2TeBr_6. Additionally, XPS scans show that no Cl ions are apparent on the surface of films (**Figure S11**). The puzzling reaction of Cs^+ ions with $TeBr_4$ and the absence of any Cl suggests a new reaction pathway. We hypothesize that $TeCl_4$ is formed as a byproduct based on DFT formation energy calculations of the overall reaction (see Supporting Information). While true $Cs_2TeCl_3Br_3$ mixed-halide single crystals have been synthesized in solution via antisolvent vapor, instead the rapid reaction while spin coating prefers Cs_2TeBr_6 and $TeCl_4$.[22] Annealing the films then sublimes $TeCl_4$ causing no chloride compounds to be detected in the film by GIWAXS. Like films made with CsBr, an increase in the concentration of CsCl results in increased $TeBr_4$ conversion. In contrast, films made with CsI show new features in diffraction patterns, indicating the presence of additional phases. While Cs_2TeBr_6 reflections are still dominant, weak scattering intensity is observed that mirrors the known (222) and (400) Cs_2TeBr_6 reflections at q = 1.99 Å^{-1} and q = 2.30 Å^{-1}, respectively, except at slightly lower q. As CsI concentration increases, these features shift to lower q and approach the position of the (222) and (400) reflections in the Cs_2TeI_6 reference powder pattern. Cs_2TeI_6 reflections are more evident in samples where a lower concentration $TeBr_4$ solution was used to cast the initial layer (**Figure S12**). This supports the existence of mixed halide octahedra in the perovskite, the quantity of which increases with increasing CsI concentration. As more iodine is incorporated, the lattice parameter of the average unit cell increases, and these reflections shift to lower q. However, this is not conclusive because this peak is in a crowded section of the diffraction pattern and therefore is hard to identify and definitively attribute to mixed halide octahedra. Additionally, this observation can be interpreted in two different ways: either increased CsI concentration induces the formation of more octahedra with the same I:Br ratio, or an increased I:Br ratio in octahedra. Photoluminescence (PL) experiments were performed to confirm the identity of mixed halide

phases. PL data shows a broad emissive peak that is characteristic of VODPs and is largely attributed to the presence of self-trapped excitons.[47,48] This peak shifts to lower energy with increased CsI concentration, supporting the presence of octahedra with an increased I:Br ratio (**Figure 4g**). Iodine's lower electronegativity than bromine reduces the optical transition energy of TeX_6^{2-} octahedra. The conduction band of tellurium-based VODPs is derived from the anti-bonding hybridization of the Te 5s and halogen np orbitals, so a less electronegative X-site halogen leads to a higher energy p orbital and consequently lower energy conduction band minimum.[21,49] The bandgap therefore shrinks, causing a redshift in the PL emission. Br and I p orbitals both contribute to the conduction band in mixed octahedra, and the bandgap is effectively tuned between both extremes. These results demonstrate the potential for two-step spin coating methods to be adapted for multi-halide alloy film growth.

Single-Carrier Device Characteristics

Our 2-step route allows us to make thin Cs_2TeBr_6 films making it easier to examine the valence band structure with photoemission. Ultraviolet photoelectron spectroscopy (UPS) was conducted to extract band energy values (**Figure S13**). We defined the onset of the VBM from a logarithmic plot because of the observed onset; we note that taking the onset from the plot on linear scale results in a value shifted deeper by X. The Fermi level (E_F) was found to be -4.99 eV, and the valence band maximum (VBM) was found to be –5.29 eV from the logarithmic plot with reference to the vacuum level. Prior estimates on the VBM position of Cs_2TeBr_6 at –5.97 eV have been made with XPS.[50] X-rays excite deeper core-level electrons, making XPS less sensitive compared to UPS, which primarily excites electrons from the valence band. We determine the Fermi level to be closer to the VBM, suggesting Cs_2TeBr_6 films are *p*-type as cast.

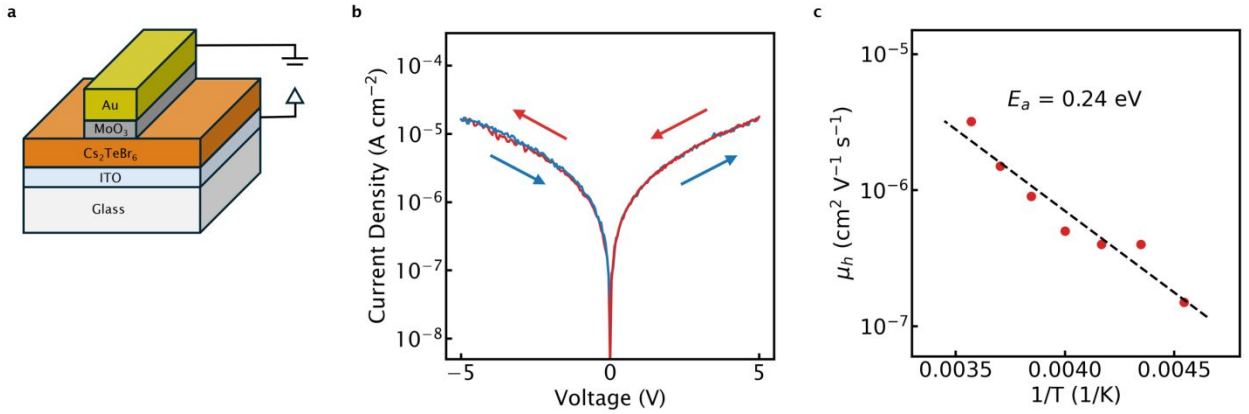

Figure 5: (a) Schematic depicting space-charge-limited current (SCLC) diode device architecture. (b) *J-V* plot for a Cs_2TeBr_6 device at 280 K. Arrows depict the direction of voltage sweep. (c) Arrhenius plot of hole mobility values from *J-V* curves acquired at different temperatures.

Enabled by thin film synthesis and VBM measurements, hole-only devices were fabricated to measure space-charge-limited hole currents in Cs_2TeBr_6 films. In contrast to Hall effect measurements, SCLC measurements reveal the behavior under conditions where injection, defect states and grain boundaries can significantly affect transport. Indium tin oxide (ITO) is chosen as the hole injecting bottom contact and gold is chosen as the top contact (**Figure 5a**). Both of these have work functions that align well with the VBM of Cs_2TeBr_6, as determined with UPS.[51,52] XPS experiments confirm that Cs_2TeBr_6 films grown on ITO-coated substrates are phase-pure (**Figure S14, Table S5**). Molybdenum oxide (MoO_3) prevents diffusion of gold through the active layer and is known to act as a hole transport layer.[53–55] *J-V* curves show low current density magnitudes consistent with the isolated nature of octahedra in VODPs (**Figure 5b**). Minimal hysteresis is observed, and injection does not strongly depend on bias direction. This agrees with the energetically well-aligned contacts and hence supports our VBM estimate. After correcting the data by subtracting shunt leakage current, we fit the J-V data with a space charge limited current model to produce a hole mobility of 3.2×10^{-5} cm^2 V^{-1} s^{-1} (**Figure S15**). The low magnitude of the observed mobility when compared to all-inorganic 3D MHPs suggests hopping transport caused by the localization of charge carriers in VODPs.[16] The relatively flat bands in calculated band structures in literature agree with this assessment.[21,22] We expected an Arrhenius temperature dependence of the mobility if hopping is the primary charge transport mechanism. *J-V* curves were collected at several temperatures between 280 K and 220 K to further observe this relation (**Figure S16**). An Arrhenius plot of hole mobilities (**Figure 5c**) reveals, an activation energy of 0.24 eV (see Supporting Information) which is reasonable for polaron hopping. The pre-factor, μ_0 = 0.35 cm^2 V^{-1} s^{-1}, can be interpreted as the high temperature limit for hole mobility in Cs_2TeBr_6. While we cannot fully rule out the influence of grain boundaries on the extracted mobility, the high temperature limit is still relatively low, however, and is again consistent with typical values for hopping transport. To our knowledge, this is the first study to successfully fabricate a single carrier diode with a VODP active layer and experimentally determine carrier mobility.

Conclusion

In this work, we demonstrate the successful fabrication of high-quality Cs_2TeBr_6 films via a two-step spin-coating process, offering a reliable method to produce lead-free vacancy-ordered double perovskites. By optimizing spin-coating parameters, we determine the conditions required for complete conversion of $TeBr_4$ to Cs_2TeBr_6 with PXRD and GIWAXS analysis. The adaptability of this method was further explored with halide mixing, revealing the selective formation of mixed-halide phases as confirmed with GIWAXS and PL. Lastly, valence band energetics are characterized by UPS and hole-only devices are fabricated that enable the observation of space-charge-limited current. These findings lay a strong foundation for the future design of multi-layer devices that leverage the unique properties of Cs_2TeBr_6 and related MHPs, offering promising alternatives for sustainable optoelectronic applications.

Acknowledgements

This work was supported by the U. S. Department of Energy, Office of Science, Basic Energy Sciences, under DE-SC0024422. The investigation made use of shared facilities of the National Science Foundation (NSF) Materials Research Science and Engineering Center (MRSEC) (NSF DMR-2308708) and the Optical Characterization Facility (DoD ARO DURIP 66886LSRIP) at UC Santa Barbara. Use was made of computational facilities purchased with support from the National Science Foundation (CNS-1725797) and administered by the Center for Scientific Computing (CSC). The CSC is supported by the California NanoSystems Institute and the Materials Research Science and Engineering Center (MRSEC; NSF DMR-2308708) at UC Santa Barbara. Use of the Stanford Synchrotron Radiation Lightsource, SLAC National Accelerator Laboratory, is supported by the U.S. Department of Energy, Office of Science, Office of Basic Energy Sciences under Contract No. DE-AC02-76SF00515. Work at the Molecular Foundry was supported by the Office of Science, Office of Basic Energy Sciences, of the U.S. Department of Energy under Contract No. DE-AC02-05CH11231.

Supporting Information

Supporting Information Available: *In-situ* optical characterization, GIWAXS 2D diffraction patterns and grazing angle dependence, spin-coating layer thickness estimate, further X-ray

diffraction phase identification, DFT methods, UPS band energy analysis, SCLC leakage current correction and Mott-Gurney fits. This material is available free of charge *via* the Internet at [URL].

AUTHOR INFORMATION

Corresponding Author

* mchabinyc@engineering.ucsb.edu

Author Contributions

The manuscript was written through contributions of all authors. O.K. synthesized the materials and fabricated films and devices with assistance from A.B. and L.T and characterized them. A.S.M. performed DFT calculations. O.K. analyzed the data. C.M.S.-F. assisted with experiment design for *in-situ* optical characterization at The Molecular Foundry. T.K. developed Python script for analyzing and plotting *in-situ* PL data. M.L.C. and L.T. assisted with device testing and analysis. O.K., A.B., M.L.C., and R.S. designed the project scope. All authors have given approval to the final version of the manuscript.

Funding Sources

DE-SC0024422, DE-AC02-05CH11231, NSF DMR–2308708, DoD ARO DURIP 66886LSRIP, CNS-1725797.

References

(1) Wu, S.; Chen, Z.; Yip, H.-L.; Jen, A. K.-Y. The Evolution and Future of Metal Halide Perovskite-Based Optoelectronic Devices. *Matter* **2021**, *4* (12), 3814–3834. https://doi.org/10.1016/j.matt.2021.10.026.

(2) Dong, H.; Ran, C.; Gao, W.; Li, M.; Xia, Y.; Huang, W. Metal Halide Perovskite for Next-Generation Optoelectronics: Progresses and Prospects. *eLight* **2023**, *3* (1), 3. https://doi.org/10.1186/s43593-022-00033-z.

(3) Chen, Y.; Yi, H. T.; Wu, X.; Haroldson, R.; Gartstein, Y. N.; Rodionov, Y. I.; Tikhonov, K. S.; Zakhidov, A.; Zhu, X.-Y.; Podzorov, V. Extended Carrier Lifetimes and Diffusion in Hybrid Perovskites Revealed by Hall Effect and Photoconductivity Measurements. *Nat Commun* **2016**, *7* (1), 12253. https://doi.org/10.1038/ncomms12253.

(4) Liu, S.; Biju, V. P.; Qi, Y.; Chen, W.; Liu, Z. Recent Progress in the Development of High-Efficiency Inverted Perovskite Solar Cells. *NPG Asia Mater* **2023**, *15* (1), 27. https://doi.org/10.1038/s41427-023-00474-z.

(5) Yang, D.; Zhao, B.; Yang, T.; Lai, R.; Lan, D.; Friend, R. H.; Di, D. Toward Stable and Efficient Perovskite Light-Emitting Diodes. *Adv Funct Materials* **2022**, *32* (9), 2109495. https://doi.org/10.1002/adfm.202109495.

(6) Bui, T. H.; Shin, J. H. Perovskite Materials for Sensing Applications: Recent Advances and Challenges. *Microchemical Journal* **2023**, *191*, 108924. https://doi.org/10.1016/j.microc.2023.108924.

(7) Xie, M.; Tian, J. Operational Stability Issues and Challenges in Metal Halide Perovskite Light-Emitting Diodes. *J. Phys. Chem. Lett.* **2022**, *13* (8), 1962–1971. https://doi.org/10.1021/acs.jpclett.1c04210.

(8) Mao, L.; Stoumpos, C. C.; Kanatzidis, M. G. Two-Dimensional Hybrid Halide Perovskites: Principles and Promises. *J. Am. Chem. Soc.* **2019**, *141* (3), 1171–1190. https://doi.org/10.1021/jacs.8b10851.

(9) Duan, D.; Ge, C.; Rahaman, M. Z.; Lin, C.-H.; Shi, Y.; Lin, H.; Hu, H.; Wu, T. Recent Progress with One-Dimensional Metal Halide Perovskites: From Rational Synthesis to Optoelectronic Applications. *NPG Asia Mater* **2023**, *15* (1), 8. https://doi.org/10.1038/s41427-023-00465-0.

(10) Huang, Z.; Proppe, A. H.; Tan, H.; Saidaminov, M. I.; Tan, F.; Mei, A.; Tan, C.-S.; Wei, M.; Hou, Y.; Han, H.; Kelley, S. O.; Sargent, E. H. Suppressed Ion Migration in Reduced-Dimensional Perovskites Improves Operating Stability. *ACS Energy Lett.* **2019**, *4* (7), 1521–1527. https://doi.org/10.1021/acsenergylett.9b00892.

(11) Cho, J.; DuBose, J. T.; Le, A. N. T.; Kamat, P. V. Suppressed Halide Ion Migration in 2D Lead Halide Perovskites. *ACS Materials Lett.* **2020**, *2* (6), 565–570. https://doi.org/10.1021/acsmaterialslett.0c00124.

(12) Lai, H.; Kan, B.; Liu, T.; Zheng, N.; Xie, Z.; Zhou, T.; Wan, X.; Zhang, X.; Liu, Y.; Chen, Y. Two-Dimensional Ruddlesden–Popper Perovskite with Nanorod-like Morphology for Solar Cells with Efficiency Exceeding 15%. *J. Am. Chem. Soc.* **2018**, *140* (37), 11639–11646. https://doi.org/10.1021/jacs.8b04604.

(13) Maughan, A. E.; Ganose, A. M.; Scanlon, D. O.; Neilson, J. R. Perspectives and Design Principles of Vacancy-Ordered Double Perovskite Halide Semiconductors. *Chem. Mater.* **2019**, *31* (4), 1184–1195. https://doi.org/10.1021/acs.chemmater.8b05036.

(14) Cai, Y.; Xie, W.; Ding, H.; Chen, Y.; Krishnamoorthy, T.; Wong, L. H.; Mathews, N.; Mhaisalkar, S. G.; Sherburne, M.; Asta, M. Computational Study of Halide Perovskite-Derived A_2BX_6 Inorganic Compounds: Chemical Trends in Electronic Structure and Structural Stability. *Chem. Mater.* **2017**, *29* (18), 7740–7749. https://doi.org/10.1021/acs.chemmater.7b02013.

(15) Maughan, A. E.; Ganose, A. M.; Candia, A. M.; Granger, J. T.; Scanlon, D. O.; Neilson, J. R. Anharmonicity and Octahedral Tilting in Hybrid Vacancy-Ordered Double Perovskites. *Chem. Mater.* **2018**, *30* (2), 472–483. https://doi.org/10.1021/acs.chemmater.7b04516.

(16) Zhang, F.; Gao, W.; Cruz, G. J.; Sun, Y.; Zhang, P.; Zhao, J. Giant Excitonic Effects in Vacancy-Ordered Double Perovskites. *Phys. Rev. B* **2023**, *107* (23), 235119. https://doi.org/10.1103/PhysRevB.107.235119.

(17) Xu, Z.; Jiang, X.; Cai, H.; Chen, K.; Yao, X.; Feng, Y. Toward a General Understanding of Exciton Self-Trapping in Metal Halide Perovskites. *J. Phys. Chem. Lett.* **2021**, *12* (43), 10472–10478. https://doi.org/10.1021/acs.jpclett.1c02291.

(18) Adhikari, M.; Shrivastava, N.; McClain, S. T.; Adhikari, C. M.; Guzelturk, B.; Khanal, R.; Gautam, B.; Luo, Z. Luminescence from Self-Trapped Excitons and Energy Transfers in Vacancy-Ordered Hexagonal Halide Perovskite Cs_2HfF_6 Doped with Rare Earths for Radiation Detection. *Advanced Optical Materials* **2022**, *10* (19), 2201374. https://doi.org/10.1002/adom.202201374.

(19) Maughan, A. E.; Ganose, A. M.; Almaker, M. A.; Scanlon, D. O.; Neilson, J. R. Tolerance Factor and Cooperative Tilting Effects in Vacancy-Ordered Double Perovskite Halides. *Chem. Mater.* **2018**, *30* (11), 3909–3919. https://doi.org/10.1021/acs.chemmater.8b01549.

(20) Bhumla, P.; Jain, M.; Sheoran, S.; Bhattacharya, S. Vacancy-Ordered Double Perovskites Cs_2BI_6 (B = Pt, Pd, Te, Sn): An Emerging Class of Thermoelectric Materials. *J. Phys. Chem. Lett.* **2022**, *13* (50), 11655–11662. https://doi.org/10.1021/acs.jpclett.2c02852.

(21) Cucco, B.; Katan, C.; Even, J.; Kepenekian, M.; Volonakis, G. Fine Structure of Excitons in Vacancy-Ordered Halide Double Perovskites. *ACS Materials Lett.* **2023**, *5* (1), 52–59. https://doi.org/10.1021/acsmaterialslett.2c01010.

(22) Folgueras, M. C.; Jin, J.; Gao, M.; Quan, L. N.; Steele, J. A.; Srivastava, S.; Ross, M. B.; Zhang, R.; Seeler, F.; Schierle-Arndt, K.; Asta, M.; Yang, P. Lattice Dynamics and Optoelectronic Properties of Vacancy-Ordered Double Perovskite Cs_2TeX_6 ($X = Cl^-, Br^-, I^-$) Single Crystals. *J. Phys. Chem. C* **2021**, *125* (45), 25126–25139. https://doi.org/10.1021/acs.jpcc.1c08332.

(23) Sajedi Alvar, M.; Blom, P. W. M.; Wetzelaer, G.-J. A. H. Space-Charge-Limited Electron and Hole Currents in Hybrid Organic-Inorganic Perovskites. *Nat Commun* **2020**, *11* (1), 4023. https://doi.org/10.1038/s41467-020-17868-0.

(24) Le Corre, V. M.; Duijnstee, E. A.; El Tambouli, O.; Ball, J. M.; Snaith, H. J.; Lim, J.; Koster, L. J. A. Revealing Charge Carrier Mobility and Defect Densities in Metal Halide Perovskites via Space-Charge-Limited Current Measurements. *ACS Energy Lett.* **2021**, *6* (3), 1087–1094. https://doi.org/10.1021/acsenergylett.0c02599.

(25) Cao, X.; Zhang, G.; Hao, L.; Ding, X.; Dong, T.; Li, X.; Zeng, Q.; He, X.; Jia, Y.; Wei, J. Achieving One-Step Solution Deposition of High Quality CsPbBr3 Films for Efficient Solar Cells through Halide Ion Exchange. *Journal of Alloys and Compounds* **2022**, *919*, 165722. https://doi.org/10.1016/j.jallcom.2022.165722.

(26) Sun, N.; Fu, S.; Li, Y.; Chen, L.; Chung, J.; Saeed, M. M.; Dolia, K.; Rahimi, A.; Li, C.; Song, Z.; Yan, Y. Tailoring Crystallization Dynamics of $CsPbI_3$ for Scalable Production of Efficient Inorganic Perovskite Solar Cells. *Adv Funct Materials* **2024**, *34* (6), 2309894. https://doi.org/10.1002/adfm.202309894.

(27) Han, Y.; Xie, H.; Lim, E. L.; Bi, D. Review of Two-Step Method for Lead Halide Perovskite Solar Cells. *Solar RRL* **2022**, *6* (6), 2101007. https://doi.org/10.1002/solr.202101007.

(28) Chauhan, M.; Zhong, Y.; Schötz, K.; Tripathi, B.; Köhler, A.; Huettner, S.; Panzer, F. Investigating Two-Step $MAPbI_3$ Thin Film Formation during Spin Coating by Simultaneous *in Situ* Absorption and Photoluminescence Spectroscopy. *J. Mater. Chem. A* **2020**, *8* (10), 5086–5094. https://doi.org/10.1039/C9TA12409H.

(29) Mohamad Noh, M. F.; Arzaee, N. A.; Nawas Mumthas, I. N.; Aadenan, A.; Saifuddin, F. H.; Syakirin, A. D. A.-G.; Abd Mutalib, M.; Lokman, M. Q.; Ibrahim, M. A.; Mat Teridi, M. A. Superiority of Two-Step Deposition over One-Step Deposition for Perovskite Solar Cells

Processed in High Humidity Atmosphere. *Optical Materials* **2021**, *118*, 111288. https://doi.org/10.1016/j.optmat.2021.111288.

(30) Folgueras, M. C.; Louisia, S.; Jin, J.; Gao, M.; Du, A.; Fakra, S. C.; Zhang, R.; Seeler, F.; Schierle-Arndt, K.; Yang, P. Ligand-Free Processable Perovskite Semiconductor Ink. *Nano Lett.* **2021**, *21* (20), 8856–8862. https://doi.org/10.1021/acs.nanolett.1c03308.

(31) Hamukwaya, S. L.; Hao, H.; Zhao, Z.; Dong, J.; Zhong, T.; Xing, J.; Hao, L.; Mashingaidze, M. M. A Review of Recent Developments in Preparation Methods for Large-Area Perovskite Solar Cells. *Coatings* **2022**, *12* (2), 252. https://doi.org/10.3390/coatings12020252.

(32) Zheng, D.; Raffin, F.; Volovitch, P.; Pauporté, T. Control of Perovskite Film Crystallization and Growth Direction to Target Homogeneous Monolithic Structures. *Nat Commun* **2022**, *13* (1), 6655. https://doi.org/10.1038/s41467-022-34332-3.

(33) Ezike, S. C.; Ahmed, A. D.; Obodo, R. M.; Salawu, M. A. Perovskite Precursor Concentration for Enhanced Recombination Suppression in Perovskite Solar Cells. *Hybrid Advances* **2022**, *1*, 100006. https://doi.org/10.1016/j.hybadv.2022.100006.

(34) Greenwood, N. N.; Straughan, B. P.; Wilson, A. E. Behaviour of Tellurium(IV) Chloride, Bromide, and Iodide in Organic Solvents and the Structures of the Species Present. *J. Chem. Soc., A* **1968**, 2209. https://doi.org/10.1039/j19680002209.

(35) Brumberg, A.; Kuklinski, O.; Kent, G. T.; Morgan, E. E.; Mikhailovsky, A. A.; Strom, T. A.; Chabinyc, M. L.; Seshadri, R. Tuning the Optical Absorption Edge of Vacancy-Ordered Double Perovskites through Metal Precursor and Solvent Selection. *Chem. Mater.* **2024**, *36* (19), 9625–9635. https://doi.org/10.1021/acs.chemmater.4c01701.

(36) Buss, B.; Krebs, B. Crystal Structure of Tellurium Tetrachloride. *Inorg. Chem.* **1971**, *10* (12), 2795–2800. https://doi.org/10.1021/ic50106a035.

(37) Jiang, J.; Niu, G.; Sui, L.; Wang, X.; Zeng, X.; Zhang, Y.; Che, L.; Wu, G.; Yuan, K.; Yang, X. Six-Photon Excited Self-Trapped Excitons Photoluminescence in Lead-Free Halide Perovskite. *Advanced Optical Materials* **2023**, *11* (5), 2202634. https://doi.org/10.1002/adom.202202634.

(38) Butkus, J.; Vashishtha, P.; Chen, K.; Gallaher, J. K.; Prasad, S. K. K.; Metin, D. Z.; Laufersky, G.; Gaston, N.; Halpert, J. E.; Hodgkiss, J. M. The Evolution of Quantum Confinement in $CsPbBr_3$ Perovskite Nanocrystals. *Chem. Mater.* **2017**, *29* (8), 3644–3652. https://doi.org/10.1021/acs.chemmater.7b00478.

(39) Steele, J. A.; Solano, E.; Hardy, D.; Dayton, D.; Ladd, D.; White, K.; Chen, P.; Hou, J.; Huang, H.; Saha, R. A.; Wang, L.; Gao, F.; Hofkens, J.; Roeffaers, M. B. J.; Chernyshov, D.; Toney, M. F. How to GIWAXS: Grazing Incidence Wide Angle X-Ray Scattering Applied to Metal Halide Perovskite Thin Films. *Advanced Energy Materials* **2023**, 2300760. https://doi.org/10.1002/aenm.202300760.

(40) D'Alessio, L.; Ferro, D.; Piacente, V. Sublimation Study of Tellurium Tetrachloride and Tetraiodide from Their Vapour Pressure Measurements. *Journal of Alloys and Compounds* **1994**, *209* (1–2), 207–212. https://doi.org/10.1016/0925-8388(94)91099-5.

(41) Shlykov, S. A.; Giricheva, N. I.; Titov, A. V.; Szwak, M.; Lentz, D.; Girichev, G. V. The Structures of Tellurium(Iv) Halides in the Gas Phase and as Solvated Molecules. *Dalton Trans.* **2010**, *39* (13), 3245. https://doi.org/10.1039/b922474b.

(42) Shlykov, S. A.; Oberhammer, H.; Titov, A. V.; Giricheva, N. I.; Girichev, G. V. A Combined Gas-Phase Electron Diffraction/Mass Spectrometric Study of the Sublimation Processes of $TeBr_4$ and TeI_4: The Molecular Structure of Tellurium Dibromide and Tellurium Diiodide. *Eur J Inorg Chem* **2008**, *2008* (33), 5220–5227. https://doi.org/10.1002/ejic.200800700.

(43) Karlsson, M.; Yi, Z.; Reichert, S.; Luo, X.; Lin, W.; Zhang, Z.; Bao, C.; Zhang, R.; Bai, S.; Zheng, G.; Teng, P.; Duan, L.; Lu, Y.; Zheng, K.; Pullerits, T.; Deibel, C.; Xu, W.; Friend, R.; Gao, F. Mixed Halide Perovskites for Spectrally Stable and High-Efficiency Blue Light-Emitting Diodes. *Nat Commun* **2021**, *12* (1), 361. https://doi.org/10.1038/s41467-020-20582-6.

(44) Wei, Q.; Ghasemi, M.; Wang, R.; Wang, C.; Wang, J.; Zhou, W.; Jia, B.; Yang, Y.; Wen, X. Metal Halide Perovskite Alloy: Fundamental, Optoelectronic Properties and Applications. *Advanced Photonics Research* **2023**, *4* (2), 2200236. https://doi.org/10.1002/adpr.202200236.

(45) Tauc, J.; Grigorovici, R.; Vancu, A. Optical Properties and Electronic Structure of Amorphous Germanium. *Physica Status Solidi (b)* **1966**, *15* (2), 627–637. https://doi.org/10.1002/pssb.19660150224.

(46) Dolgonos, A.; Mason, T. O.; Poeppelmeier, K. R. Direct Optical Band Gap Measurement in Polycrystalline Semiconductors: A Critical Look at the Tauc Method. *Journal of Solid State Chemistry* **2016**, *240*, 43–48. https://doi.org/10.1016/j.jssc.2016.05.010.

(47) Guo, Q.; Zhao, X.; Song, B.; Luo, J.; Tang, J. Light Emission of Self-Trapped Excitons in Inorganic Metal Halides for Optoelectronic Applications. *Advanced Materials* **2022**, *34* (52), 2201008. https://doi.org/10.1002/adma.202201008.

(48) Li, S.; Luo, J.; Liu, J.; Tang, J. Self-Trapped Excitons in All-Inorganic Halide Perovskites: Fundamentals, Status, and Potential Applications. *J. Phys. Chem. Lett.* **2019**, *10* (8), 1999–2007. https://doi.org/10.1021/acs.jpclett.8b03604.

(49) Pal, B.; Kale, A. J.; Sharma, M.; Bhamu, K. C.; Kang, S. G.; Singh, V. K.; Dixit, A. Inorganic Cs_2TeX_6 (X = Cl, Br, I) Lead-Free Vacancy-Ordered Double-Perovskite Absorber-Based Single-Junction Solar Cells with a Higher Efficiency of ~24%: Theoretical Insights. *Energy Fuels* **2024**, acs.energyfuels.3c03030. https://doi.org/10.1021/acs.energyfuels.3c03030.

(50) Jin, J.; Chen, C.; Smith, P. W.; Folgueras, M. C.; Yu, S.; Zhang, Y.; Chen, P.-C.; Seeler, F.; Schaefer, B.; Lizandara-Pueyo, C.; Zhang, R.; Schierle-Arndt, K.; Yang, P. Benzyl Alcohol Photo-Oxidation Based on Molecular Electronic Transitions in Metal Halide Perovskites. *ACS Photonics* **2023**, *10* (3), 772–779. https://doi.org/10.1021/acsphotonics.3c00042.

(51) Sachtler, W. M. H.; Dorgelo, G. J. H.; Holscher, A. A. The Work Function of Gold. *Surface Science* **1966**, *5* (2), 221–229. https://doi.org/10.1016/0039-6028(66)90083-5.

(52) Park, Y.; Choong, V.; Gao, Y.; Hsieh, B. R.; Tang, C. W. Work Function of Indium Tin Oxide Transparent Conductor Measured by Photoelectron Spectroscopy. *Applied Physics Letters* **1996**, *68* (19), 2699–2701. https://doi.org/10.1063/1.116313.

(53) Avigad, E.; Etgar, L. Studying the Effect of MoO_3 in Hole-Conductor-Free Perovskite Solar Cells. *ACS Energy Lett.* **2018**, *3* (9), 2240–2245. https://doi.org/10.1021/acsenergylett.8b01169.

(54) Dasgupta, B.; Goh, W. P.; Ooi, Z. E.; Wong, L. M.; Jiang, C. Y.; Ren, Y.; Tok, E. S.; Pan, J.; Zhang, J.; Chiam, S. Y. Enhanced Extraction Rates through Gap States of Molybdenum Oxide Anode Buffer. *J. Phys. Chem. C* **2013**, *117* (18), 9206–9211. https://doi.org/10.1021/jp3114013.

(55) Sun, S.; Xu, M.; Zhang, Y.; Liu, R.; Wang, X.; Zhang, L.; Fang, Y.; Wang, P. Study of Molybdenum Oxide Optimized Hole Carrier Transport in Perovskite Solar Cells. *Organic Electronics* **2023**, *113*, 106697. https://doi.org/10.1016/j.orgel.2022.106697.

Data for this article, including X-ray scattering, spectroscopic data, and electronic transport data, are available at the Dryad Repository at: https://doi.org/ 10.5061/dryad.qnk98sfv0